Hindawi
Journal of Nanomaterials
Volume 2022, Article ID 5062752, 16 pages
https://doi.org/10.1155/2022/5062752

Research Article

Green Ca-Loaded MgO Nanoparticles as an Efficient Adsorbent for Organic Hazardous Dyes

Noha Al-Awaji,[1] Moufida Boukriba,[2] Abuzar Albadri,[1] Mohamed Ali Ben Aissa,[2] Mohamed Bououdina,[3] and Abueliz Modwi[2]

[1]*Department of Chemistry, College of Science, Qassim University, Buraidah 51452, Saudi Arabia*
[2]*Department of Chemistry, College of Science and Arts at Al-Rass, Qassim University, Saudi Arabia*
[3]*Department of Mathematics and Science, Faculty of Humanities and Sciences, Prince Sultan University, Riyadh, Saudi Arabia*

Correspondence should be addressed to Mohamed Bououdina; mboudina@gmail.com
and Abueliz Modwi; abuelizkh81@gmail.com

Received 22 June 2022; Accepted 18 August 2022; Published 2 September 2022

Academic Editor: Ngoc Thinh Nguyen

Textile industry wastewater is a principal source of environmental contamination, posing serious health and environmental risks; consequently, appropriate treatments are necessary before ultimate discharge to ensure environmental and public health safety. In this study, 10% Ca-doped MgO ($Ca_{0.10}Mg_{0.90}O$) has been prepared via a green and ecologically benign approach using aqueous solution of gum arabic (GA) and then used to eliminate Congo red (CR) from aqueous solution. The XRD analysis reveals a size reduction of MgO nanoparticles from 11 to 6 nm after doping with a surface area reaching 50.1 $m^2 \cdot g^{-1}$ for the synthesized heterostructure. An excellent adsorption efficiency of 97% has been achieved under the following optimal operational conditions, i.e., adsorbent dosage of $Ca_{0.10}Mg_{0.90}O$ (0.400 g/L), contact time of 120 min, and solution pH of 7.00. As indicated by pH, isotherm, and FTIR examinations, the CR sorption process is related to chemisorption and hydrogen bonding. The findings indicate that the synthesized nanomaterial is a suitable candidate for dyes containing effluent treatment due to its facile green synthetic approach using a natural product GA, low-cost, mesoporous nature, and high uptake capacity under neutral solution pH.

1. Introduction

Water is regarded as a vital resource for the survival of life on earth. The textile industry has contaminated clean water supplies for decades [1]. The use of synthetic dyes throughout the industrial processes results in massive wastewater effluents discharged into the environment on a daily basis [2]. Synthetic organic dyes, such as Congo red (CR), are resistant to the biodegradation, and thus, they are hazardous to the environment and human health [3–6]. Congo red dye ($C_{32}H_{22}N_6Na_2O_6S_2$) is a class of dyes mostly utilized to color industrial items and hence discharged in significant amounts into water resources [7]. CR dyes cause serious environmental and health concerns; the most prevalent are cancer, gene mutation, and lung and kidney diseases [8].

In this context, numerous viable solutions have been developed for treating CR-contaminated waters and minimizing their further discharge into water resources [9–11]. Diverse physical and chemical processes for the removal of organic dyes have been proposed, including Fenton oxidation [12], biological approaches [13], membrane separation [14], electrochemical oxidation [15], photocatalysis [16], and electrocoagulation. Nonetheless, adsorption methods have gained considerable attention, thanks to their simplicity, low cost, and effectiveness [6, 17].

Nanostructured materials exhibit appreciably novel and improved chemical, biological, and physical properties [18], which can be tuned by chemical composition (doping, composites), particle's shape and size, surface treatment, and functionalization. The observed outstanding and unique

properties at the nanoscale are associated with quantum confinement, surface plasmonic resonance, and surface-to-volume ratio (surface area). Hence, nanoparticles have found widespread applications in various fields, including photocatalysis [19], wastewater treatment [20], and air purification [21].

Magnesium oxide (MgO) with its rock-salt cubic structure (Fm-3 m space group no. 225) possesses interesting properties such as good thermal conductivity, transparency to infrared, chemical stability, and excellent corrosion resistance [22]. Besides, it offers broad range of usage in fuel cells, supercapacitors, paints, batteries, ceramics, catalysts, and electronics [23, 24]. MgO nanoparticles have also been tested as an effective adsorbent to remove heavy metals and organic dyes from contaminated waters [25, 26].

MgO was synthesized using different methods, such as sonochemical route [27], chemical vapor deposition [28], precipitation [29], hydrothermal [30], microwave [31], combustion [32], and carbothermic reduction [33]. Sol-gel is a simple and common method already adopted to synthesize MgO nanostructures, since it manifests a high yield with minimal temperature requirement [34]. Furthermore, doping of metal oxide nanomaterials has been reported as an effective approach for the removal of dyes from contaminated waters by adsorption or photodegradation. Indeed, it was found that doping modifies and tunes markedly nanomaterial's properties, notably the porosity and surface area, and consequently improves the sorption capacity and kinetics. Due to the existence of polysaccharides (galactosyl, arabinosyl, rhamnosyl, glucuronosyl, and 4-O-methyl-glucuronosyl) which are competent reducing agents, gum arabic (GA) was employed as a reducing dispersing agent to prepare nanostructures with enhanced properties to achieve high performance in diverse applications, specifically the elimination of hazardous organic and inorganic pollutants from contaminated wastewaters [35, 36].

Nowadays, green technologies attract great interest for environmental protection. In this study, aqueous solution of gum arabic has been used as a natural stabilizing and capping agent for the green synthesis of Ca-loaded MgO ($Ca_{0.10}Mg_{0.90}O$) nanoparticles and then evaluated for the adsorption of Congo red dye. Microstructural, structural, and surface area and pore size and functional groups are checked by SEM, XRD, BET, and FTIR analyses. The influence of operational parameters, such as dye dose, contact time, and pH on sorption capability, has been examined. Besides, kinetic and adsorption isotherm experiments were conducted. The possible mechanism of CR dye removal by Ca-doped MgO nanoparticles was proposed.

2. Experimental Procedures

2.1. Chemicals. Magnesium carbonate dehydrate (≥99.0%), calcium carbonate (≥98.0%), sodium chloride (NaCl, ≥99%), sodium hydroxide (NaOH, ≥99%), hydrochloric acid (HCl, 37%), Congo red (CR, ≥ 97.0%), basic fuchsin (BF, ≥85%), malachite green (MG, ≥90%), crystal violet (CV, ≥90%), methyl orange (MO, ≥85%), and methylene blue (MB, ≥82%) purchased from Merck Company were used without further purification. Gum arabic (*Acacia senegal*) with the required concentrations (5 to 100 ppm) was obtained by diluting CR stock solution (200 ppm).

2.2. Material's Preparation. The Ca-doped MgO 10% ($Ca_{0.10}Mg_{0.90}O$) nanoparticles were synthesized via the sol-gel method. First, 21 g of magnesium carbonate dehydrate ($MgCO_3$) and 2.5 g of calcium carbonate ($CaCO_3$) were dissolved in 500 mL of distilled water (DW). Then, 125 mL of NaOH ethanolic solution (0.02 M) was added dropwise while sonicating for 30 min. After that, 25 mL of gum arabic (*Acacia senegal*) solution (5 g in 100 mL of DW) was added and sonicated for 15 min. The mixture was left 24 h; subsequently, the as-formed white gel was washed thoroughly with DW and dried at 90°C for 5 h. The formed product was then calcined at 700°C for 120 min. The same procedure was repeated by taking similar quantities of the reagents without adding $CaCO_3$ to synthesize MgO nanoparticles.

2.3. Characterizations. Scanning electron microscopy (SEM) was used to examine the morphology of the as-prepared powders using a JEOL JEM-6700F apparatus equipped with electron dispersive X-ray spectroscopy (EDS) to determine the elemental chemical composition. X-ray diffraction (XRD) was used to check the phase purity and the crystal structure using a Rigaku Mini Flex 600 (Tokyo, Japan) diffractometer equipped with a CuKα radiation source ($\lambda = 1.5418$ Å). A Micrometrics ASAP 2020 analyzer was used to determine the surface area and pore size of the fabricated nanopowders. The Brunauer-Emmett-Teller (BET) formula and Lippens and de Boer's t-plot approach were used to determined nanopowders' surface area and porosity. A JASCO FT-IR spectrometer was used to study the vibration modes of $Ca_{0.10}Mg_{0.90}O$ nanoparticles before and after CR dye adsorption.

2.4. Adsorption and Kinetic Studies. The sorption process was utilized to estimate the CR dye removal rate by $Ca_{0.10}Mg_{0.90}O$ nanopowders. For the kinetic and contact time experiments, 150 mL of CR dye solution with 150 ppm initial concentration was mixed with 60 mg of $Ca_{0.10}Mg_{0.90}O_2$ nanopowders. A small suspension volume was removed at defined periods of time and then centrifuged to estimate the remaining CR dye quantity using a LABOMED UVS-2800 spectrophotometer. The residual CR concentration was obtained at a maximum wavelength of 497 nm, and the quantity of CR dye extracted per gram of sorbent $Ca_{0.10}Mg_{0.90}O_2$ at any interval (min) is calculated using the following formula [37]:

$$Q_t = \frac{(C_i - C_t)V}{w}, \quad (1)$$

where Q_t (in mg·g^{-1}) is the capacity of CR dye removed per mass of sorbent (w (g)) at each time t (min), C_i and C_t represent the concentrations of CR dye (in ppm) before and after adding CR ultimately at any time, and V is the CR dye volume (L).

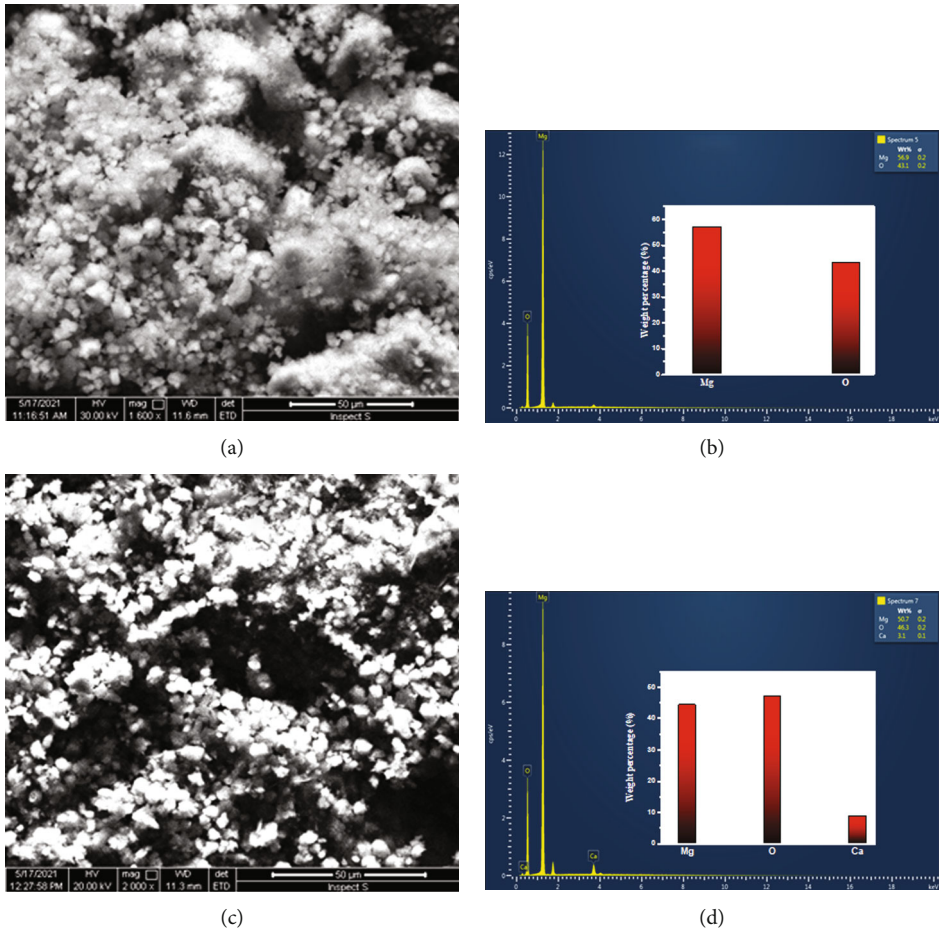

Figure 1: SEM images and corresponding EDX spectrum of MgO (a–c) and $Ca_{0.10}Mg_{0.90}O$ nanoparticles (b–d).

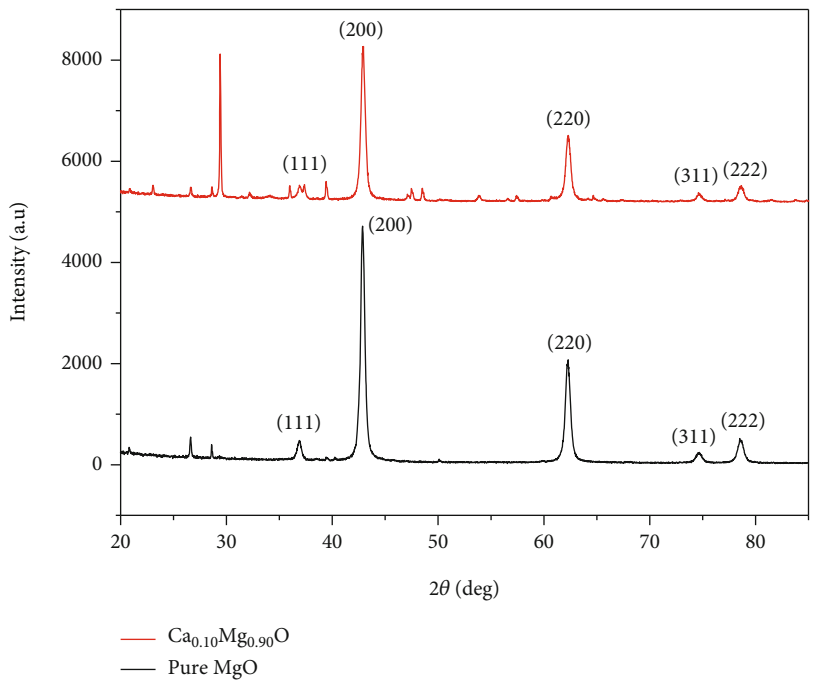

Figure 2: XRD patterns of MgO and $Ca_{0.10}Mg_{0.90}O$ nanopowders.

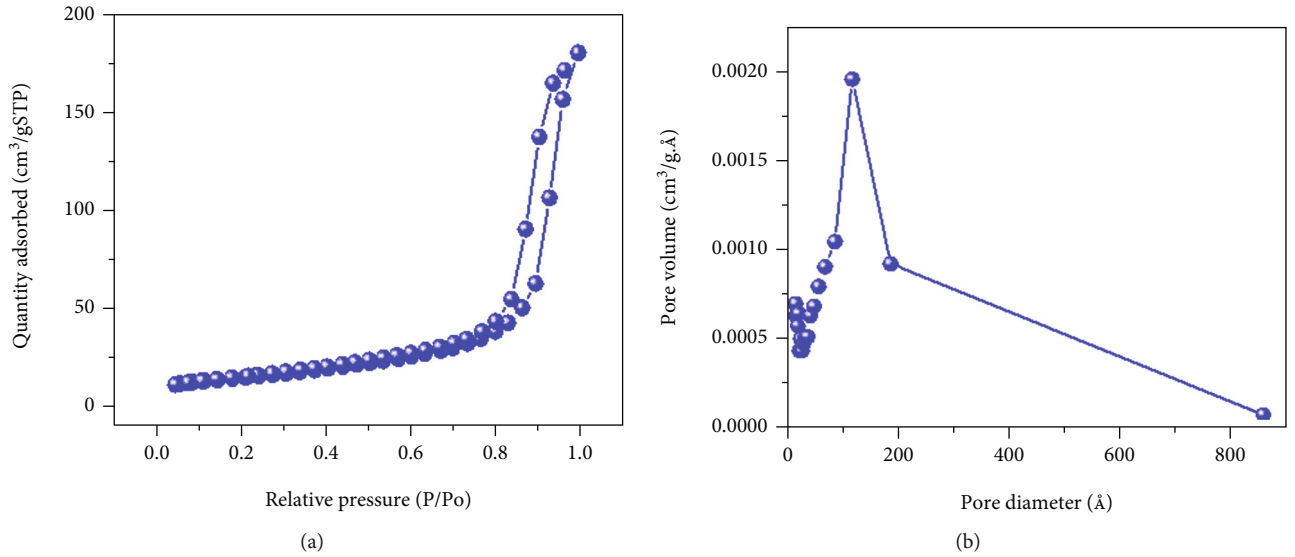

Figure 3: (a) Nitrogen adsorption-desorption isotherm and (b) pore size distribution of $Ca_{0.10}Mg_{0.90}O$ nanopowders.

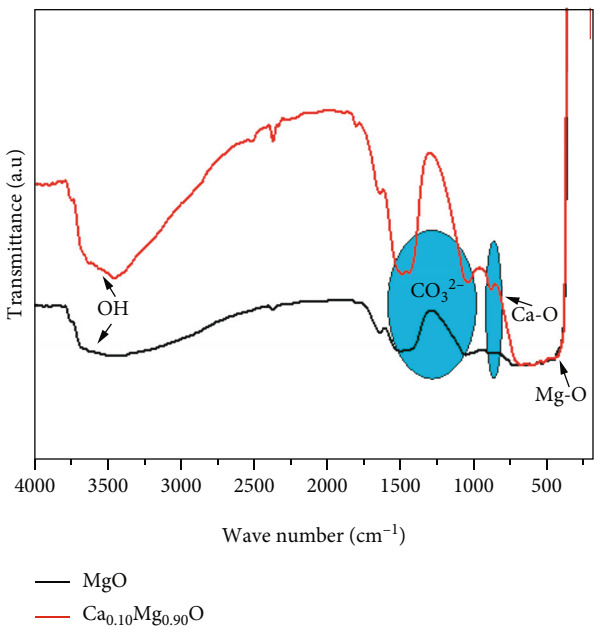

Figure 4: FTIR spectra of MgO and $Ca_{0.10}Mg_{0.90}O$ nanopowders.

The equilibrium removal experiment was carried out in a 25 mL glass vial containing 10 mg of sorbent material, and 25 mL of CR dye with varying concentrations (25, 50, 100, 150, 250, and 300 ppm) was enrolled under a magnetic agitation for 1440 min. Following the removal equilibrium study, the mixture was then centrifuged and separated, whereby the remaining CR concentration was calculated as follows [38]:

$$Q_e = \frac{(C_i - C_e)V}{w}, \quad (2)$$

where Q_e ($mg{\cdot}g^{-1}$) is the capacity of CR dye eliminated through the mass of sorbent nanopowders and C_e is the CR dye concentration at equilibrium in $mg{\cdot}L^{-1}$. After the sorption experiment, the utilized $Ca_{0.10}Mg_{0.90}O$ nanopowders have been recovered by filtration and subsequently calcined at 773 K for 2 h. After that, the collected $Ca_{0.10}Mg_{0.90}O$ nanopowders have been utilized for additional adsorption tests.

3. Results and Discussion

3.1. $Ca_{0.10}Mg_{0.90}O$ Nanoparticle Description. MgO and $Ca_{0.10}Mg_{0.90}O$ SEM images are presented in Figure 1. SEM images of MgO (Figure 1(a)) and Ca-doped MgO (Figure 1(b)) show irregular spherical crystallized particles with a mean diameter ≈ 100 nm. EDX spectra display intense signals at 1.2 and 0.5 keV related to Mg and O for MgO (Figure 1(c)) and 3.7, 1.2, and 0.5 keV corresponding to Ca, Mg, and O for $Ca_{0.10}Mg_{0.90}O$ (Figure 1(d)). This confirms the formation of Ca-doped MgO nanoparticles without the presence of any impurities. The weight proportions of the elements determined from the EDX analysis provided as an inset in Figures 1(c) and 1(d) are consistent with the starting chemical composition.

The phase purity of MgO and $Ca_{0.10}Mg_{0.90}O$ nanopowders was determined by XRD analysis (see Figure 2). The principal peaks located at $2\theta = 36.9°$, 42.9°, 62.2°, 74.6°, and 78.6° correspond, respectively, to (111), (200), (220), (311), and (222) reflections of MgO face-centered cubic-FCC phase ($Fm\bar{3}m$, 225, $a = 4.213$ Å) with a rock salt-type structure [39], in agreement with JCPDS No. 87-0653. Two minor peaks located at $2\theta = 36.9°$ and 42.9° are associated with organic molecules of the gum arabic extract [40].

For $Ca_{0.10}Mg_{0.90}O$, the XRD pattern manifests similar diffraction peaks with a slight shift towards higher 2θ angles, indicating a contraction of the unit cell of MgO crystal structure. Meanwhile, two additional peaks located at $2\theta = 32.3°$ and 53.9° are indexed as (110) and (433) reflections, respectively, belonging to the CaO phase with a cubic structure ($Fm\bar{3}m$, 225, $a = 4.801$ Å) [41] .

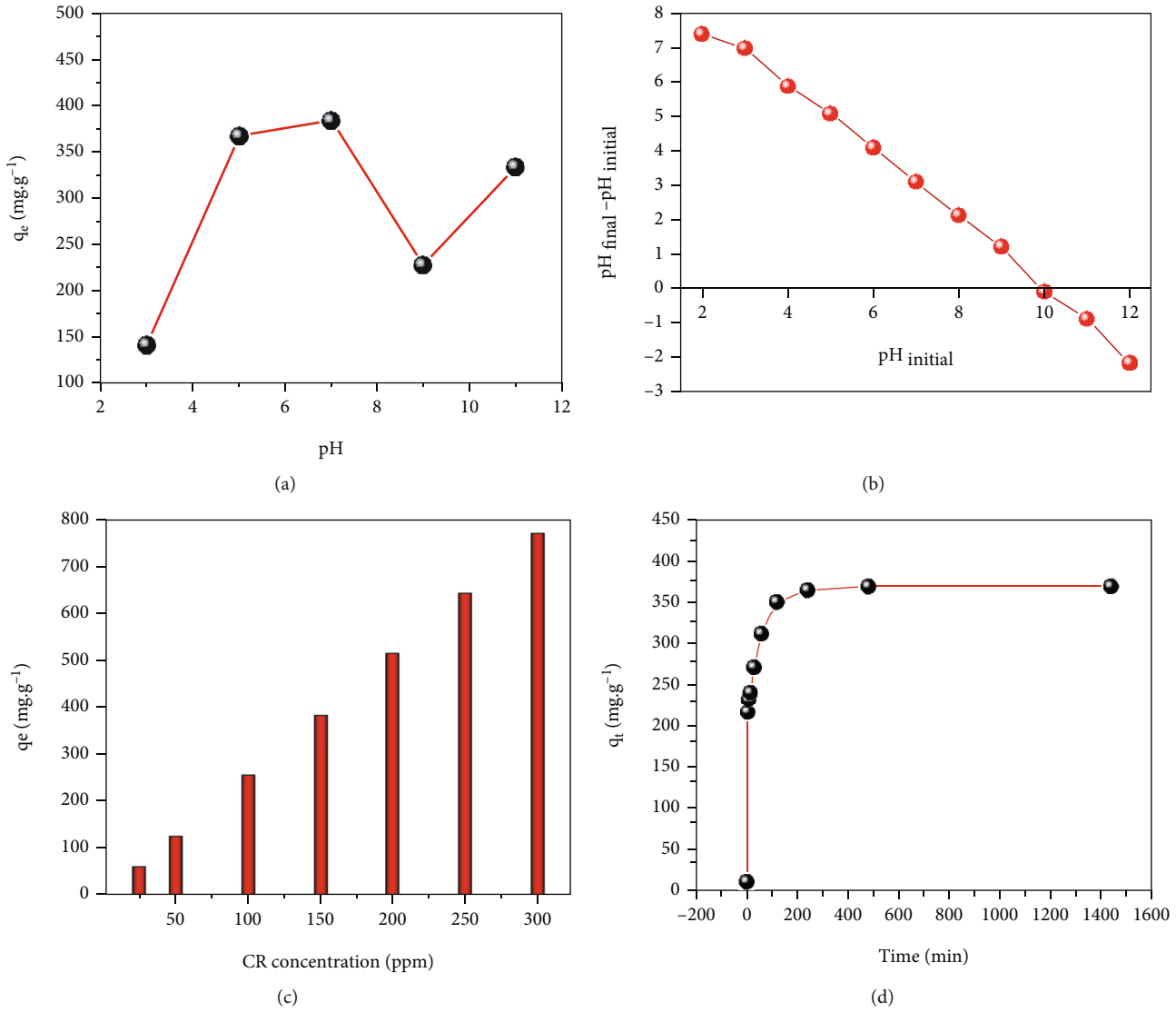

FIGURE 5: (a) Influence of pH on CR % removal for initial dye concentration of 100 ppm, (b) plot for the pH_{PZC} for $Ca_{0.10}Mg_{0.90}O$, (c) impact of the initial CR concentration at pH = 7, and (d) contact time on the sorption rate onto $Ca_{0.10}Mg_{0.90}O$ nanoparticles for initial dye concentration of 150 ppm and pH = 7.

The calculated values of the crystallite size are 10.93 nm for pure MgO and then reduced by almost half with 10% Ca doping reaching 5.98 nm. The obtained smaller particle size can contribute to the increased total surface area per unit volume and enhance the diffusion of dye molecules from the bulk solution toward the solid phase. Because the active sites exposed to the surrounding are greatly increased with reduced particle size, besides the interior surface of particles may be available for adsorption in comparison to larger size particles [42]. However, both values of the microstrain are found negative, i.e., -2.4×10^{-3}% and -5.6×10^{-3}% for MgO and $Ca_{0.10}Mg_{0.90}O$, respectively. The as-obtained compressive microstrain (negative values) may be explained by the existence of oxygen and magnesium vacancies inside the crystal structure of MgO.

The lattice parameter a of the MgO phase has been calculated using the main diffraction peak (200) by using the following expression:

$$a = \frac{\lambda}{2 \sin \theta} \sqrt{h^2 + k^2 + l^2}, \quad (3)$$

where d is the interplanar distance, θ is the diffraction angle, λ the wavelength of the X-ray source (1.5418 Å), and (h, k, l) are Miller indices of the diffraction peak. The calculated lattice constants for MgO and $Ca_{0.10}Mg_{0.90}O$ are found to be 4.5337 and 4.5304 Å, respectively. It is noted that the calculated MgO lattice parameter is lower than the rock salt bulk phase value reported in the literature [43], which may be due to insufficient oxygen/magnesium interstitials, self-interstitials substituting oxygen with magnesium, and di-interstitials.

Furthermore, it is important to mention that the incorporation of Ca ions into MgO host lattice by occupying

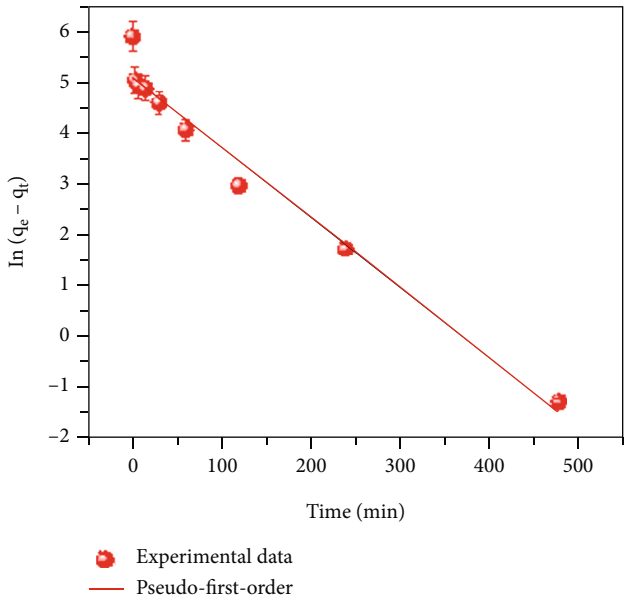

(a)

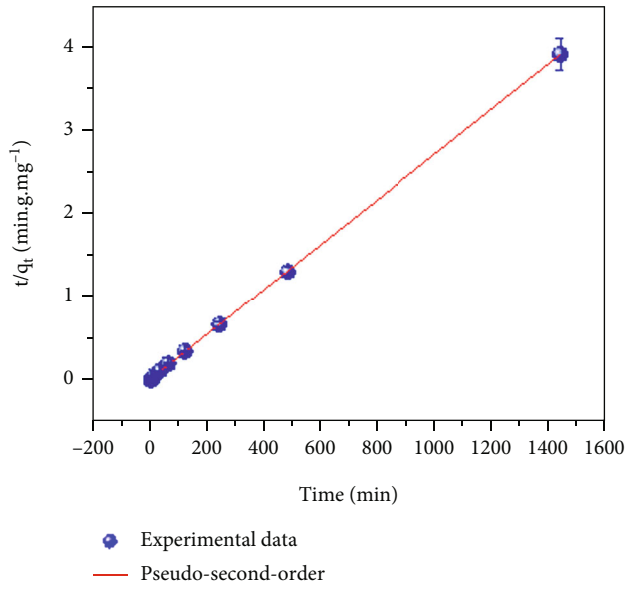

(b)

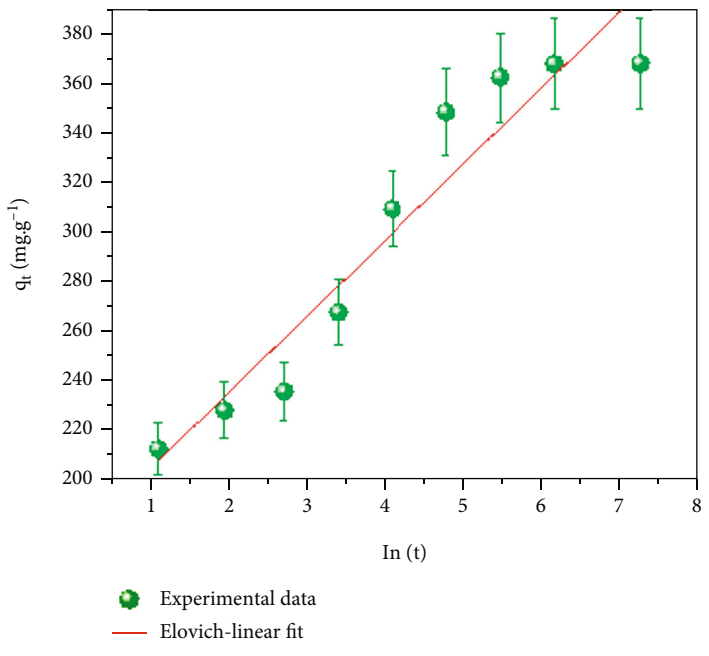

(c)

Figure 6: Continued.

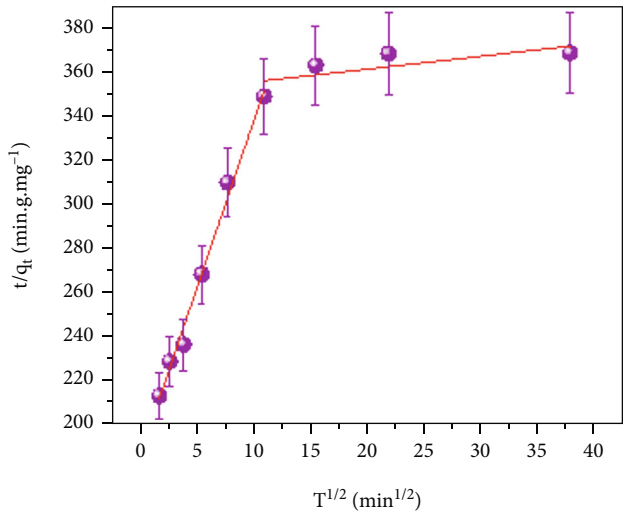

(d)

FIGURE 6: PFO (a), PSO (b), Elovich models (c) for CR sorption onto $Ca_{0.10}Mg_{0.90}O$ nanoparticles, and (d) intraparticle diffusion plots for CR adsorption by $Ca_{0.10}Mg_{0.90}O$ nanoparticles for initial dye concentration of 150 ppm and pH = 7.

TABLE 1: Kinetic models for CR sorption onto $Ca_{0.10}Mg_{0.90}O$ nanoparticles.

Kinetic model	Kinetic equation	Parameters	Values
PFO [53]	$\ln(q_e - q_t) = \ln q_e - k_1 t$	$\mathbf{q_e}$ (mg/g)	166 ± 1.32
		K_1 (min^{-1})	$13.7 \times 10^{-3} \pm 0.19$
		$\mathbf{R^2}$	0.97
PSO [53]	$\frac{t}{q_t} = \left[\frac{1}{k_2 q_e^2}\right] + \frac{1}{q_e} t$	$\mathbf{q_m}$ (exp) (mg/g)	130.7 ± 1.19
		$\mathbf{q_m}$ (cal) (mg/g)	370
		$\mathbf{K_2}$ (g/mg·min)	$0.45 \times 10^{-3} \pm 0.39$
		$\mathbf{h_0}$ ($mg \cdot g^{-1} \cdot min^{-1}$)	61.6
		$\boldsymbol{t_{1/2}}$ (min)	0.166
		$\mathbf{R^2}$	0.99
Elovich [54]	$q_t = \frac{1}{\beta} \ln(\alpha\beta) + \frac{1}{\beta} \ln t$	$\boldsymbol{\beta}$	0.032 ± 0.58
		$\boldsymbol{\alpha}$	8192 ± 0.62
		$\mathbf{R^2}$	0.92
Intraparticle diffusion [54]	$q_t = k_{dif} t^{1/2} + C$	K_{dif1} ($mg \cdot min^{1/2}/g$)	15.22
		C_1	184.85
		$\mathbf{R^2}$	0.98
		K_{dif2} ($mg \cdot min^{1/2}/g$)	0.58
		C_2	349.57
		$\boldsymbol{R^2}$	0.55

Mg sites would be accompanied by an expansion of the unit cell, since Ca^{2+} possesses higher ionic radius (0.99 Å) compared to Mg^{2+} (0.65 Å). However, it is noticed that the value of the lattice parameter of $Ca_{0.10}Mg_{0.90}O$ (4.5304 Å) is slightly lower than that of pure MgO (4.5337 Å). This discrepancy can be explained by lattice distortion upon partial substitution of much larger Ca ions replacing smaller Mg ions and the possibility of the formation of oxygen vacancies during the synthesis process.

N_2 adsorption-desorption curves have been recorded to examine the nature of the microstructure and determine the surface area and mean pore size of $Ca_{0.10}Mg_{0.90}O$ (see Figure 3). The isotherm (Figure 3(a)) manifests type V, suggesting that the presence of mesopores in phase change like pore condensation could occur [44]. The $Ca_{0.10}Mg_{0.90}O$ BET surface area is found to be around 50.1 $m^2 \cdot g^{-1}$ with a pore distribution and volume of 11.79 nm and 0.277 $cm^3 g^{-1}$, respectively (Figure 3(b)).

Table 2: Isotherm models for CR sorption onto $Ca_{0.10}Mg_{0.90}O$ nanoparticles.

Equilibrium model	Linear form	Parameters	Values
Langmuir [55]	$\frac{C_e}{q_e} = \frac{1}{q_m K_L} + \frac{C_e}{q_m}$	$\mathbf{q_m}$ (mg/g)	526 ± 4.94
		$\mathbf{K_L}$ (mg/g)	$0.528 \pm 1.21 \times 10^{-3}$
		$\mathbf{R_L}$ (L/mg)	0.006
		$\mathbf{R}^2$	0.98
Freundlich [56]	$\ln q_e = \ln K_F + \frac{1}{n} \ln C_e$	n	0.752 ± 0.123
		$\mathbf{K_F}$ (L/mg)	35.95 ± 2.86
		$\mathbf{R}^2$	0.96
Dubinin-Radushkevich [57]	$q_e = \frac{\mathrm{RT}}{b} \ln K_T + \frac{\mathrm{RT}}{b} \ln C_e$	$\mathbf{q_m}$ (mg/g)	457 ± 17.61
		$\boldsymbol{\beta} \times 10^{-9}$ (mol/kJ)^2	$7.84 \pm 1.13 \times 10^{-5}$
		$\mathbf{E}$ (KJ/mol)	17.43 ± 11.12
		$\mathbf{R}^2$	0.95
Temkin [58]	$\ln q_e = \ln q_m - K\varepsilon^2$	$\mathbf{B}$ (J/mol)	6.418 ± 5.21
		$\mathbf{K_T}$ (L/mg)	4.29 ± 0.145
		$\boldsymbol{R}^2$	0.92

FTIR analysis has been performed to determine the chemical bonds and composition (purity) of the prepared compounds (see Figure 4). FTIR spectra display a broad band at 3465 cm^{-1} assigned to the stretching vibration of the O–H group [45], whereas the band at 1639 cm^{-1} is ascribed to the adsorbed water molecule's -OH stretching mode. In addition, the three bands observed at 1524, 1406, and 1056 cm^{-1} are related to a unidentate carbonate adsorbed on the surface of nanoparticles [46]. The characteristic band located at 420 cm^{-1} is assigned to Mg–O vibration mode [47], hence confirming the formation of the MgO phase. Furthermore, the appearance of a band at 871 cm^{-1} is associated with CaO stretching [48], hence asserting the incorporation of Ca within the MgO host lattice, in accordance with XRD analysis.

3.2. Adsorption Measurements

3.2.1. Effect of pH, Initial CR Concentration, and Contact Time. The pH value plays a critical role in the adsorption mechanism because it influences the sorbent's surface charge hence enabling the adsorption of the dye molecules. The adsorption of CR onto $Ca_{0.10}Mg_{0.90}O$ has been evaluated at pH value varying in the range 3 to 11 (see Figure 5(a)). It is noted that the adsorption efficiency increases markedly when the pH value increases in the acidic medium range (3 to 7) and then decreases at basic pH values. The zero-point charge experiment has been conducted to better elucidate the adsorption mechanism in terms of surface charge effect. From Figure 5(b), the point zero charges (pH_{PZC}) of $Ca_{0.10}Mg_{0.90}O$ have been estimated; i.e., its value is found to be 10. Thus, its surface is positively charged at pH below 10 and negatively charged above pH 10. Hence, it can be deduced that when the pH is increased, the $Ca_{0.10}Mg_{0.90}O$ surface becomes negatively charged, resulting in an electrostatic repulsion between the $Ca_{0.10}Mg_{0.90}O$ surface and the anionic CR dye molecules, and consequently, a reduced adsorption rate is attained. The decrease in the adsorption capacity of CR in the alkaline pH might be attributed to the excess OH^- and the anionic CR ($-SO_3^-$) competition [49] as well as the hydrolysis of MgO in basic medium.

In addition, the influence of CR dye concentration on the amount of dye adsorbed is examined. Figure 5(c) indicates that when the concentration of CR dye is raised gradually from 25 up to 300 mg. L^{-1}, the CR adsorption rate increases significantly and linearly from 63.2 up to 769.2 mg·g^{-1}, respectively. Herein, it can be observed that increasing the initial concentration of CR generates an efficient force that overcomes any resistance to CR migration.

3.3. Contact Time and Kinetic Studies. The effect of equilibrium time for the CR adsorption onto $Ca_{0.10}Mg_{0.90}O$ nanoparticles has been examined for a fixed CR initial concentration of 150 ppm over an agitation time in the range 5-1440 min (see Figure 5(d)). The elimination of the CR is enhanced with the contact time and reaches the equilibrium within 120 min. The adsorption rate is found to increase significantly during the first few min of the process ($h_0 = 61.6\,\mathrm{mg} \cdot \mathrm{g}^{-1} \cdot \mathrm{min}^{-1}$), due to the accessibility of many active sites available onto $Ca_{0.10}Mg_{0.90}O$ nanoparticles' surface. Eventually, the concentration of the active sites falls once approaching the equilibrium resulting in a lower sorption rate; hence, the CR molecules' removal remains almost unchanged.

A kinetic study for the CR elimination by $Ca_{0.10}Mg_{0.90}O$ nanoparticles has been carried out for a sorbent dose of 500 mg/L and $[CR]_0 = 150$ ppm, while varying the contact time at 5, 10, 20, 40, 80, and 120 min. Four models, namely, pseudo-first-order (PFO), pseudo-second-order (PSO), intraparticle diffusion, and Elovich models, have been adopted to elucidate the adsorption kinetics; as shown in Figure 6, the relevant equations and the obtained results

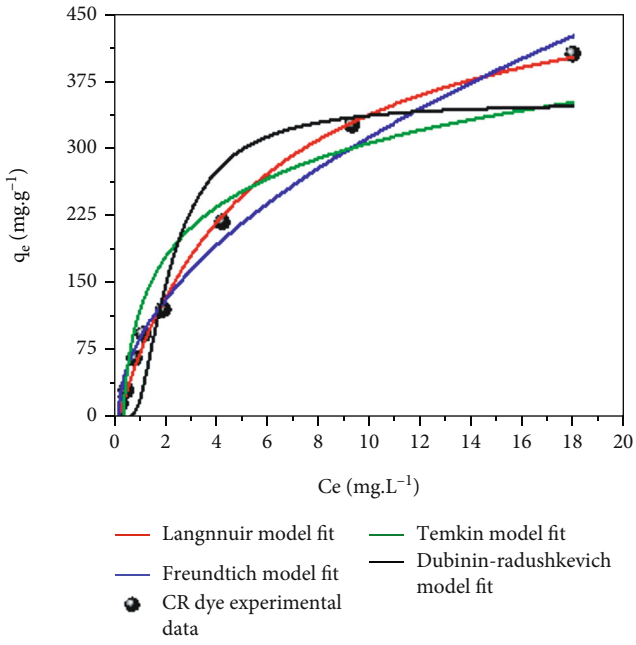

(a)

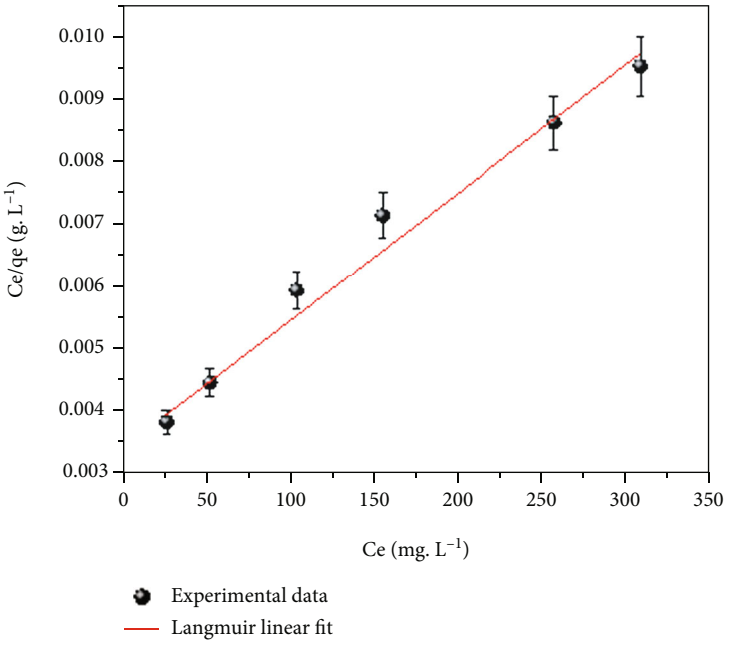

(b)

Figure 7: Continued.

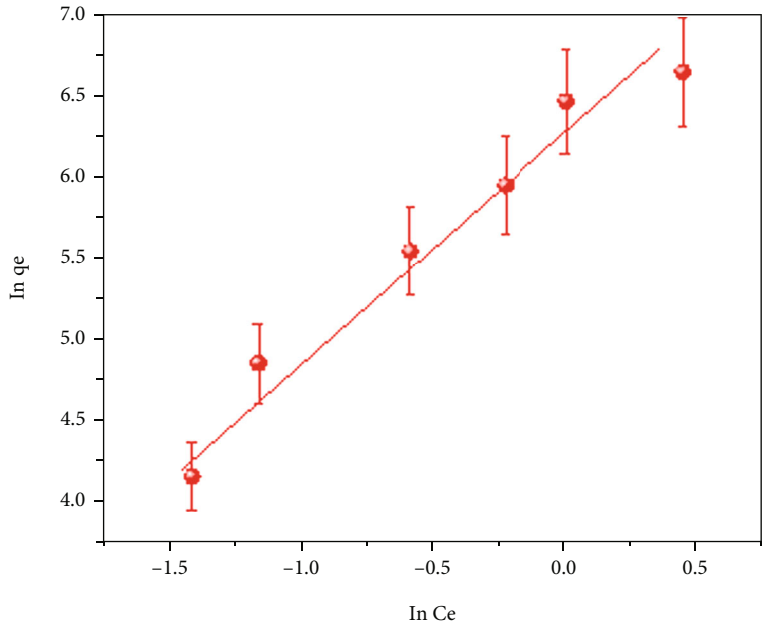

(c)

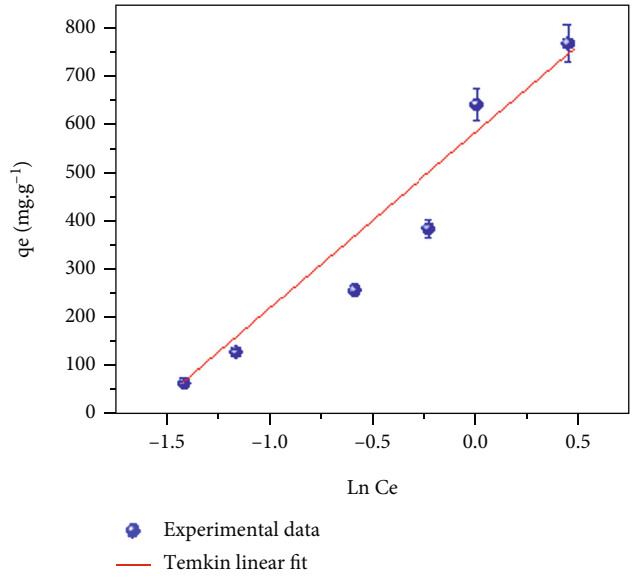

(d)

Figure 7: Continued.

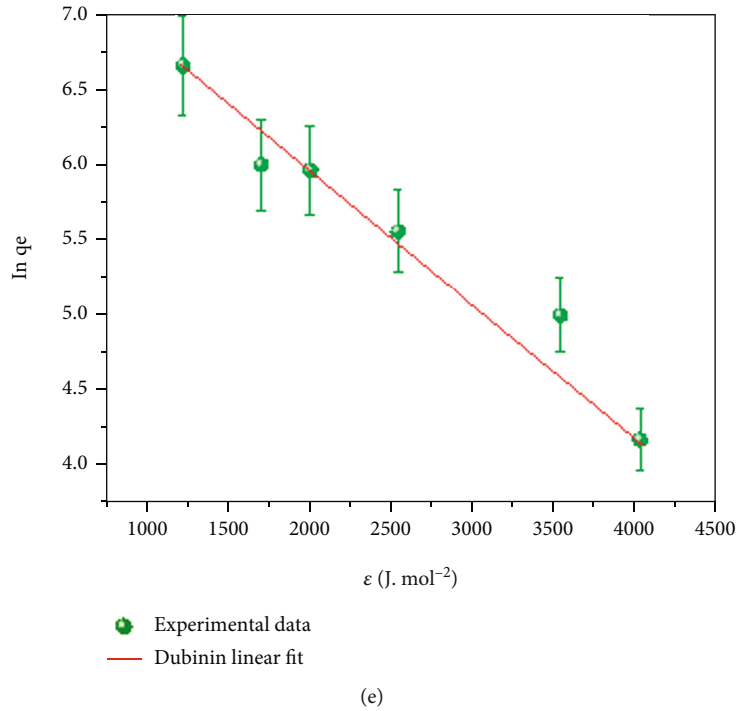

(e)

Figure 7: Adsorption of CR equilibrium data fitted using (a) nonlinear models and (b) Langmuir, (c) Freundlich, (d) Temkin, and (e) Dubinin-Radushkevich models at pH = 7.

Table 3: Sorption capacity of various sorbents for the CR removal as reported in the literature.

Adsorbents	Adsorption capacity (mg/g)	Time (min)	Reference
MgO nanoplates	131	30	[61]
Hierarchical hollow Fe_2O_3	160	25	[62]
Co_3O_4@Fe_3O_4 hollow spheres	125	20	[63]
Jujuba seeds	56	100	[64]
Porous alumina	370	30	[65]
Zinc curcumin oxide	94	70	[66]
Porous ZnO microspheres	334	180	[60]
Fe_3O_4@bacteria	320	30	[67]
Polypyrrole-iron oxide	500	40	[59]
$Ca_{0.10}Mg_{0.90}O$ nanoparticles	526	110	Present study

(the kinetic parameters k_1 and k_2 and the correlation coefficient R^2) are given in Table 1. It can be noted that the R^2 value obtained from the PSO plots ($R^2 = 0.9998$) is greater than that obtained from the PFO model ($R^2 = 0.8615$), manifesting that the kinetics and the sorption process fit extremely well with the PSO model. Moreover, the adsorption capacity assessed using the PSO curve ($\mathbf{q_m} = 370\,\mathrm{mg \cdot g^{-1}}$) is very close with the experimental value ($\mathbf{q_m} = 365\,\mathrm{mg \cdot g^{-1}}$).

Through the intraparticle transport/diffusion mechanism, the CR dye molecules may be transported from the solution to the surface of $Ca_{0.10}Mg_{0.90}O$ nanoparticles [50] (see Figure 6(d)). It can be observed that the adsorption process occurs upon two distinct stages [51]. The first stage reflects the transport of CR molecules from the bulk solution through the boundary layer to the surface of $Ca_{0.10}Mg_{0.90}O$ nanoparticles [52], whereas the second stage manifests the equilibrium state in which intraparticle diffusion starts to diminish due to low CR concentration [52].

3.4. Adsorption Equilibrium Study. One of the furthermost important characteristics to evaluate the adsorption ability of $Ca_{0.10}Mg_{0.90}O$ nanoparticles is the CR maximum quantity (Q_{max}). The adsorption data has been fitted using different isotherms to estimate the uptake capacity of $Ca_{0.10}Mg_{0.90}O$ nanoparticles. Dubinin-Radushkevich, Freundlich-Langmuir, and Temkin's adsorption models are examined at equilibrium under isothermal conditions. The corresponding formulas of the used isotherm models and the computed parameters are given in Table 2.

The isotherm graphs for CR elimination by $Ca_{0.10}Mg_{0.90}O$ nanoparticles are illustrated in Figure 7. It can be observed from the fitting curves and the data reported in Table 2 that the Langmuir isotherm model has the highest R^2 (0.98). The equilibrium value of $\mathbf{R_L}$ is approximately 0.006, indicating a favorable equilibrium adsorption. These results demonstrate that the Langmuir isotherm model provides the most accurate match to the experimental data. According to the Langmuir isotherm model, the maximum sorption capacity of $Ca_{0.10}Mg_{0.90}O$ nanoparticles for CR dye is $526\,\mathrm{mg \times g^{-1}}$ (Table 2).

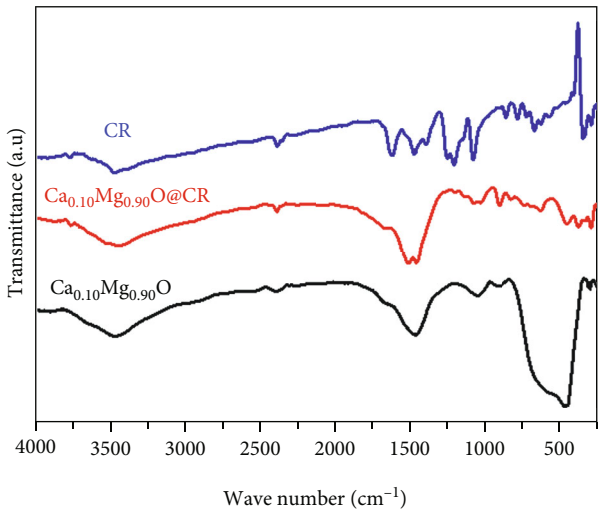

(a)

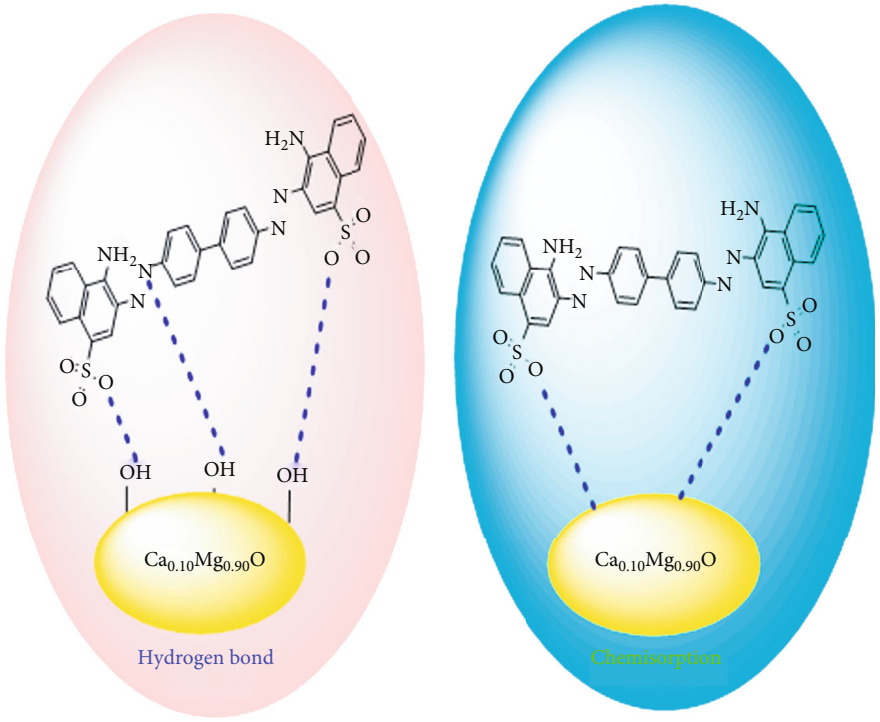

(b)

Figure 8: (a) FTIR spectra of $Ca_{0.10}Mg_{0.90}O$, CR, and $Ca_{0.10}Mg_{0.90}O$@CR and (b) the proposed sorption mechanism of CR onto $Ca_{0.10}Mg_{0.90}O$.

Table 4: FTIR characteristic bands for $Ca_{0.10}Mg_{0.90}O$, $Ca_{0.10}Mg_{0.90}O$@CR, and CR.

Vibration modes	CR (cm^{-1})	$Ca_{0.10}Mg_{0.90}O$ (cm^{-1})	$Ca_{0.10}Mg_{0.90}O$@CR (cm^{-1})
OH stretching	—	3460	3452
N–H stretching	3475	—	3454
N=N stretching	1594	—	1581
C=C stretching	1445	—	1420
C–N bonding	1363	—	1359
SO_3^- stretching	1220, 1178, and 1119	—	1212, 1136, and 1061
Ring vibrations	833	—	831

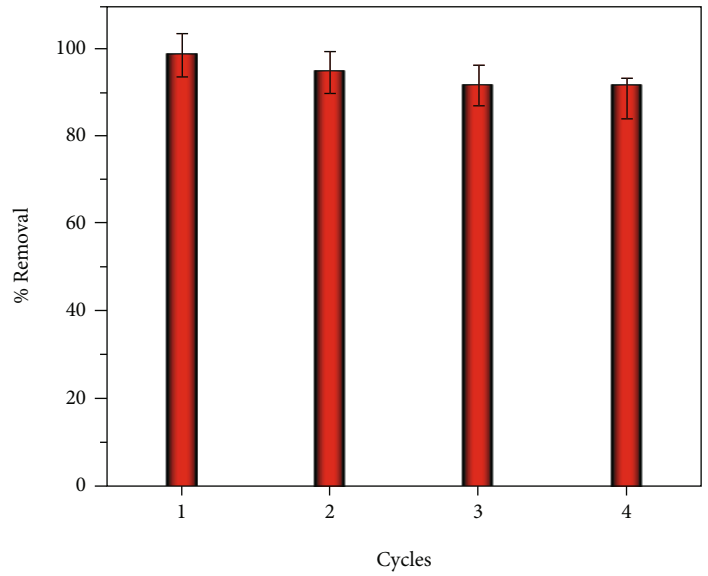

Figure 9: Reusability study of $Ca_{0.10}Mg_{0.90}O$ nanopowders.

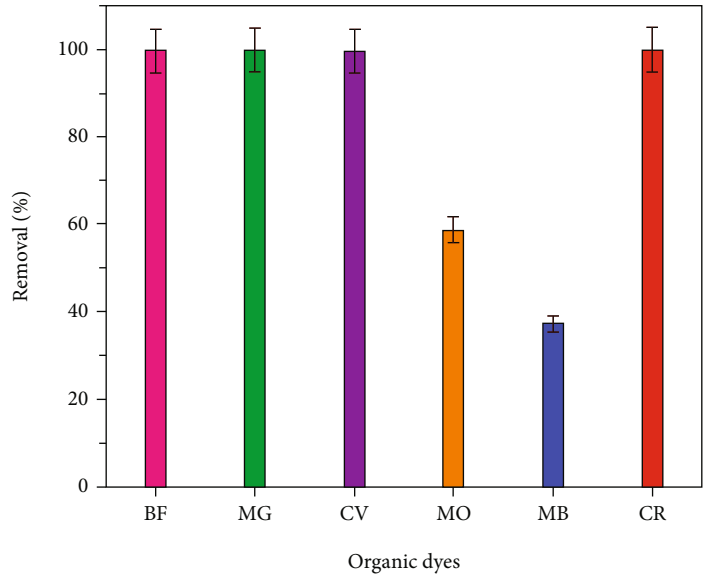

Figure 10: Adsorption ability of $Ca_{0.10}Mg_{0.90}O$ nanopowders.

3.5. Comparison Study. The ability of $Ca_{0.10}Mg_{0.90}O$ nanoparticles to adsorb CR dye molecules has been compared to that of other sorbents previously reported in the literature. As seen in Table 3, the produced $Ca_{0.10}Mg_{0.90}O$ nanoparticles exhibit a greater capacity for CR adsorption than the previously reported sorbents, indicating its potential as a promising nanosorbent for the elimination of hazardous organic dyes from wastewaters. Indeed, Sarojini et al. successfully obtained the polypyrrole-iron oxide for CR dye adsorption from aqueous solutions [59]. The achieved capacity of 500 mg/g is slightly lower compared to the value obtained in this study. Lei et al. investigated the elimination of CR from an aqueous solution by adsorption onto porous ZnO microspheres [60]. The maximum adsorption capacity was found to be 334 mg/g, which is very lower than that of $Ca_{0.10}Mg_{0.90}O$ nanopowders.

3.6. Adsorption Mechanism. To elucidate the adsorption mechanism, FTIR measurements of $Ca_{0.10}Mg_{0.90}O$ nanopowders have been recorded before and after CR adsorption in addition to the CR dye (see Figure 8(a)). The corresponding bands for $Ca_{0.10}Mg_{0.90}O$, $Ca_{0.10}Mg_{0.90}O$@CR, and CR are given in Table 4.

As seen in Figure 8(a) and Table 4, the characteristic bands of CR dye are also present in the spectrum of $Ca_{0.10}Mg_{0.90}O$ after adsorption alongside some changes in the position and the relative intensity compared to the free CR bands. After CR adsorption, the stretching O–H band shifts slightly to 3452 cm^{-1} due to the hydrogen bond formed between the amine groups of CR and the OH groups of moisture present at $Ca_{0.10}Mg_{0.90}O$ nanoparticles' surface [68]. Additionally, the SO_3^- stretching bands shift to lower

wavenumbers, indicating the occurrence of a bonding between $Ca_{0.10}Mg_{0.90}O$ particles' surface functional groups and CR dye molecules. The adsorption mechanism can be predicted by the energy value (E) in the D-R isothermal model. If the value of $E > 8\,kJ \cdot mol^{-1}$, the adsorption mechanism is principally chemical. If the value of $E < 8\,kJ \cdot mol^{-1}$, it indicates that the physical forces greatly affect the adsorption process [69]. The calculated energy value is found to be 17.43 kJ/mol, hence suggesting that CR molecules are chemisorbed-adsorbed onto the $Ca_{0.10}Mg_{0.90}O$ surface. Rahali et al. established theoretically and experimentally that CR is chemosorbed onto Ba-doped ZnO [7]. The possible sorption mechanism of CR onto $Ca_{0.10}Mg_{0.90}O$ nanoparticles' surface is illustrated in Figure 8(b).

3.7. Reusability Study of the Sorbent $Ca_{0.10}Mg_{0.90}O$. The regeneration and the reusability of an adsorbent are key features when considering scale-up and industrial applications. In this regard, it is necessary to test the cyclic viability of $Ca_{0.10}Mg_{0.90}O$ nanoparticles. The reusability performance results, as shown in Figure 9, indicate that $Ca_{0.10}Mg_{0.90}O$ nanoparticles demonstrate effective four adsorption/desorption cycles for CR removal with a mean value of 89%.

3.8. Adsorption Ability of $Ca_{0.10}Mg_{0.90}O$ for Other Organic Contaminants. The high adsorption capacity of $Ca_{0.10}Mg_{0.90}O$ for CR dye has been also examined and compared to other organic dyes (BF, CV, MG, MO, and MB), as illustrated in Figure 10 under the previous optimal operating conditions and using 50 ppm dye solution. It is readily apparent that $Ca_{0.10}Mg_{0.90}O$ nanoparticles demonstrate a high selectivity for BF, CV MG, and CR and low removal rate for both MB and MO dyes, i.e., 99.9, 99.8, 99.6, 99.4, 58.6, and 37.3% toward CR, MG, BF, CV, MO, and MB, respectively. It can be concluded that the as-prepared $Ca_{0.10}Mg_{0.90}O$ is an efficient sorbent for the removal of BF, MG, CV, and CR dyes from wastewater.

4. Conclusion

A Ca-doped MgO ($Ca_{0.10}Mg_{0.90}O$) nanosorbent was successfully prepared by a green and ecologically benign approach using aqueous solution of natural gum arabic (GA) and exhibited a high efficacy for the removal of CR dye. Batch experiments revealed that the removal of CR dye by $Ca_{0.10}Mg_{0.90}O$ was pH-dependent, with the highest adsorption capacity of 526 mg/g achieved at pH = 7. Equilibrium and kinetic modelling of the experimental data indicated that the sorption of CR by $Ca_{0.10}Mg_{0.90}O$ followed the pseudo-first-order kinetics and Langmuir adsorption isotherm models. Based on pH (zero-point charge) and FTIR measurements, the CR adsorption mechanism occurred through the chemisorption and hydrogen bonding. The investigation of $Ca_{0.10}Mg_{0.90}O$ nanopowder as adsorbents for different dyes (MB, MO, CV, BF, and MG) revealed the overall significant potential of the nanosorbent for hazardous dyes' elimination from wastewaters.

Data Availability

All data and information recorded or analyzed throughout this study are included in this paper.

Conflicts of Interest

The authors declare they have no financial interests.

Acknowledgments

The authors would like to thank the support of the Department of Chemistry, College of Science and Arts, Al-Rass, Qassim University, and also would like to thank Prince Sultan University for their support.

References

[1] H. Yuan, L. Chen, Z. Cao, and F. F. Hong, "Enhanced decolourization efficiency of textile dye reactive blue 19 in a horizontal rotating reactor using strips of BNC-immobilized laccase: optimization of conditions and comparison of decolourization efficiency," *Biochemical Engineering Journal*, vol. 156, article 107501, 2020.

[2] S. Soni, P. K. Bajpai, J. Mittal, and C. Arora, "Utilisation of cobalt doped iron based MOF for enhanced removal and recovery of methylene blue dye from waste water," *Journal of Molecular Liquids*, vol. 314, article 113642, 2020.

[3] K. Zare, H. Sadegh, R. Shahryari-ghoshekandi et al., "Enhanced removal of toxic Congo red dye using multi walled carbon nanotubes: kinetic, equilibrium studies and its comparison with other adsorbents," *Journal of Molecular Liquids*, vol. 212, pp. 266–271, 2015.

[4] Y. Zhou, J. Lu, Y. Zhou, and Y. Liu, "Recent advances for dyes removal using novel adsorbents: a review," *Environmental Pollution*, vol. 252, pp. 352–365, 2019.

[5] L. Bulgariu, L. B. Escudero, O. S. Bello et al., "The utilization of leaf-based adsorbents for dyes removal: a review," *Journal of Molecular Liquids*, vol. 276, pp. 728–747, 2019.

[6] S. Praveen, J. Jegan, T. Bhagavathi Pushpa, R. Gokulan, and L. Bulgariu, "Biochar for removal of dyes in contaminated water: an overview," *Biochar*, vol. 4, no. 1, pp. 1–16, 2022.

[7] S. Rahali, M. A. Ben Aissa, L. Khezami, N. Elamin, M. Seydou, and A. Modwi, "Adsorption behavior of Congo red onto barium-doped ZnO nanoparticles: correlation between experimental results and DFT calculations," *Langmuir*, vol. 37, no. 24, pp. 7285–7294, 2021.

[8] H. G. Elias, "Plastics, general survey in Ullmann's encyclopedia of industrial chemistry," Wiley–VCH, Weinheim, 2005.

[9] K. Z. Elwakeel, "Magnesium sorption onto titan yellow supported on classic thiourea-formaldehyde resin," *Aswan University Journal of Environmental Studies*, vol. 1, no. 2, pp. 125–136, 2020.

[10] A. Elgarahy, K. Z. Elwakeel, S. H. Mohammad, and G. A. Elshoubaky, "A critical review of biosorption of dyes, heavy metals and metalloids from wastewater as an efficient and green process," *Cleaner Engineering and Technology*, vol. 4, article 100209, 2021.

[11] R. A. Mashabi, Z. A. Khan, and K. Z. Elwakeel, "Chitosan- or glycidyl methacrylate-based adsorbents for the removal of dyes from aqueous solutions: a review," *Advances*, vol. 3, no. 14, pp. 5645–5671, 2022.

[12] E. E. Ebrahiem, M. N. Al-Maghrabi, and A. R. Mobarki, "Removal of organic pollutants from industrial wastewater by applying photo-Fenton oxidation technology," *Arabian Journal of Chemistry*, vol. 10, pp. S1674–S1679, 2017.

[13] X. Zhang, M. Liu, X. Zhang, and T. Tan, "Microbial lipid production and organic matters removal from cellulosic ethanol wastewater through coupling oleaginous yeasts and activated sludge biological method," *Bioresource Technology*, vol. 267, pp. 395–400, 2018.

[14] A. Prasannan, J. Udomsin, H. C. Tsai, C. F. Wang, and J. Y. Lai, "Robust underwater superoleophobic membranes with bio-inspired carrageenan/laponite multilayers for the effective removal of emulsions, metal ions, and organic dyes from wastewater," *Chemical Engineering Journal*, vol. 391, article 123585, 2020.

[15] M. Hassan, N. Pous, B. Xie, J. Colprim, M. D. Balaguer, and S. Puig, "Employing microbial electrochemical technology-driven electro-Fenton oxidation for the removal of recalcitrant organics from sanitary landfill leachate," *Bioresource Technology*, vol. 243, pp. 949–956, 2017.

[16] A. Modwi, B. Aissa, K. K. Taha et al., "Fabrication of (Y 2 O 3) n–ZnO nanocomposites by high-energy milling as potential photocatalysts," *Journal of Materials Science: Materials in Electronics*, vol. 32, no. 3, pp. 3415–3430, 2021.

[17] K. Z. Elwakeel, A. M. Elgarahy, and E. Guibal, "A biogenic tunable sorbent produced from upcycling of aquatic biota-based materials functionalized with methylene blue dye for the removal of chromium(VI) ions," *Journal of Environmental Chemical Engineering*, vol. 9, no. 2, article 104767, 2021.

[18] M. Gholami, M. Shirzad-Siboni, and J.-K. Yang, "Application of Ni-doped ZnO rods for the degradation of an azo dye from aqueous solutions," *Korean Journal of Chemical Engineering*, vol. 33, no. 3, pp. 812–822, 2016.

[19] L. Liu, X. Zhang, L. Yang, L. Ren, D. Wang, and J. Ye, "Metal nanoparticles induced photocatalysis," *National Science Review*, vol. 4, no. 5, pp. 761–780, 2017.

[20] C. Zhang, Z. Hu, P. Li, and S. Gajaraj, "Governing factors affecting the impacts of silver nanoparticles on wastewater treatment," *Science of the Total Environment*, vol. 572, pp. 852–873, 2016.

[21] A. H. Mamaghani, F. Haghighat, and C.-S. Lee, "Photocatalytic oxidation technology for indoor environment air purification: the state-of-the-art," *Applied Catalysis B: Environmental*, vol. 203, pp. 247–269, 2017.

[22] A. Modwi, L. Khezami, K. K. Taha, and H. Idriss, "Flower buds like MgO nanoparticles: from characterisation to indigo carmine elimination," *Zeitschrift für Naturforschung A*, vol. 73, no. 11, pp. 975–983, 2018.

[23] N. M. Julkapli and S. Bagheri, "Magnesium oxide as a heterogeneous catalyst support," *Reviews in Inorganic Chemistry*, vol. 36, no. 1, pp. 1–41, 2016.

[24] M. Shahid, C. He, S. Sankarasubramanian, V. Ramani, and S. Basu, "Enhanced methane electrooxidation by ceria and nickel oxide impregnated perovskite anodes in solid oxide fuel cells," *International Journal of Hydrogen Energy*, vol. 45, no. 19, pp. 11287–11296, 2020.

[25] S. Abinaya, H. P. Kavitha, M. Prakash, and A. Muthukrishnaraj, "Green synthesis of magnesium oxide nanoparticles and its applications: a review," *Sustainable Chemistry and Pharmacy*, vol. 19, article 100368, 2021.

[26] R. Dobrucka, "Synthesis of MgO nanoparticles using Artemisia abrotanum herba extract and their antioxidant and photocatalytic properties," *Iranian Journal of Science and Technology, Transactions A: Science*, vol. 42, no. 2, pp. 547–555, 2018.

[27] M. A. Alavi and A. Morsali, "Syntheses and characterization of $Mg(OH)_2$ and MgO nanostructures by ultrasonic method," *Ultrasonics Sonochemistry*, vol. 17, no. 2, pp. 441–446, 2010.

[28] H. Li, M. Li, X. Wang, X. Wu, F. Liu, and B. Yang, "Synthesis and optical properties of single-crystal MgO nanobelts," *Materials Letters*, vol. 102-103, pp. 80–82, 2013.

[29] D. C. Prado, I. Fernández, and J. E. Rodríguez-Páez, "MgO nanostructures: synthesis, characterization and tentative mechanisms of nanoparticles formation," *Nano-Structures & Nano-Objects*, vol. 23, article 100482, 2020.

[30] L. Kumari, W. Z. Li, C. H. Vannoy, R. M. Leblanc, and D. Z. Wang, "Synthesis, characterization and optical properties of $Mg(OH)_2$ micro-/nanostructure and its conversion to MgO," *Ceramics International*, vol. 35, no. 8, pp. 3355–3364, 2009.

[31] R. Al-Gaashani, S. Radiman, Y. Al-Douri, N. Tabet, and A. R. Daud, "Investigation of the optical properties of $Mg(OH)_2$ and MgO nanostructures obtained by microwave-assisted methods," *Journal of Alloys and Compounds*, vol. 521, pp. 71–76, 2012.

[32] N. C. S. Selvam, R. T. Kumar, L. J. Kennedy, and J. J. Vijaya, "Comparative study of microwave and conventional methods for the preparation and optical properties of novel MgO-micro and nano-structures," *Journal of Alloys and Compounds*, vol. 509, no. 41, pp. 9809–9815, 2011.

[33] M. Nusheh, H. Yoozbashizadeh, M. Askari, H. Kobatake, and H. Fukuyama, "Mechanically activated synthesis of single crystalline MgO nanostructures," *Journal of Alloys and Compounds*, vol. 506, no. 2, pp. 715–720, 2010.

[34] C. W. Wong, Y. S. Chan, J. Jeevanandam et al., "Response surface methodology optimization of mono-dispersed MgO nanoparticles fabricated by ultrasonic-assisted sol–gel method for outstanding antimicrobial and antibiofilm activities," *Journal of Cluster Science*, vol. 31, no. 2, pp. 367–389, 2020.

[35] O. Idris, P. Williams, and G. Phillips, "Characterisation of gum from *Acacia senegal* trees of different age and location using multidetection gel permeation chromatography," *Food Hydrocolloids*, vol. 12, no. 4, pp. 379–388, 1998.

[36] K. Taha, R. H. Elmahi, E. A. Hassan, S. E. Ahmed, and M. H. Shyoub, "Analytical study on three types of gum from Sudan," *Journal of Forest Products & Industries*, vol. 1, no. 1, pp. 11–16, 2012.

[37] A. Modwi, M. A. Abbo, E. A. Hassan, O. K. al-Duaij, and A. Houas, "Adsorption kinetics and photocatalytic degradation of malachite green (MG) via Cu/ZnO nanocomposites," *Journal of Environmental Chemical Engineering*, vol. 5, no. 6, pp. 5954–5960, 2017.

[38] L. Khezami, K. K. Taha, and A. Modwi, "Efficient removal of cobalt from aqueous solution by zinc oxide nanoparticles: kinetic and thermodynamic studies," *Zeitschrift für Naturforschung A*, vol. 72, no. 5, pp. 409–418, 2017.

[39] G. N. Kopanati, S. Seethamraju, P. C. Ramamurthy, and G. Madras, "A Surlyn/magnesium oxide nanocomposite as an effective water vapor barrier for organic device encapsulation," *RSC Advances*, vol. 5, no. 41, pp. 32580–32587, 2015.

[40] M. Bashir and S. Haripriya, "Assessment of physical and structural characteristics of almond gum," *International Journal of Biological Macromolecules*, vol. 93, pp. 476–482, 2016.

[41] A. Roy, S. S. Gauri, M. Bhattacharya, and J. Bhattacharya, "Antimicrobial activity of CaO nanoparticles," *Journal of Biomedical Nanotechnology*, vol. 9, no. 9, pp. 1570–1578, 2013.

[42] A. Shukla, Y. H. Zhang, P. Dubey, J. L. Margrave, and S. S. Shukla, "The role of sawdust in the removal of unwanted materials from water," *Journal of Hazardous Materials*, vol. 95, no. 1-2, pp. 137–152, 2002.

[43] S. Kaneko, T. Nagano, K. Akiyama et al., "Large constriction of lattice constant in epitaxial magnesium oxide thin film: effect of point defects on lattice constant," *Journal of Applied Physics*, vol. 107, no. 7, article 073523, 2010.

[44] V. J. Inglezakis, S. G. Poulopoulos, and H. Kazemian, "Insights into the S-shaped sorption isotherms and their dimensionless forms," *Microporous and Mesoporous Materials*, vol. 272, pp. 166–176, 2018.

[45] S. Xu, Z. Zhong, W. Liu, H. Deng, and Z. Lin, "Removal of Sb(III) from wastewater by magnesium oxide and the related mechanisms," *Environmental Research*, vol. 186, article 109489, 2020.

[46] P.-Y. Wu, Y. P. Jiang, Q. Y. Zhang, Y. Jia, D. Y. Peng, and W. Xu, "Comparative study on arsenate removal mechanism of MgO and MgO/TiO_2 composites: FTIR and XPS analysis," *New Journal of Chemistry*, vol. 40, no. 3, pp. 2878–2885, 2016.

[47] S. Taghavi Fardood, A. Ramazani, and S. Woo Joo, "Eco-friendly synthesis of magnesium oxide nanoparticles using arabic gum," *Journal of Applied Chemical Research*, vol. 12, no. 1, pp. 8–15, 2018.

[48] Y. Y. Margaretha, H. S. Prastyo, A. Ayucitra, and S. Ismadji, "Calcium oxide from Pomacea sp. shell as a catalyst for biodiesel production," *Engineering*, vol. 3, no. 1, pp. 1–9, 2012.

[49] A. N. Kani, E. Dovi, A. A. Aryee et al., "Polyethyleneimine modified tiger nut residue for removal of Congo red from solution," *Desalination and Water Treatment*, vol. 215, pp. 209–221, 2021.

[50] A. El-Sikaily, A. El Nemr, A. Khaled, and O. Abdelwehab, "Removal of toxic chromium from wastewater using green alga *Ulva lactuca* and its activated carbon," *Journal of Hazardous Materials*, vol. 148, no. 1-2, pp. 216–228, 2007.

[51] B. Royer, N. F. Cardoso, E. C. Lima et al., "Applications of Brazilian pine-fruit shell in natural and carbonized forms as adsorbents to removal of methylene blue from aqueous solutions–kinetic and equilibrium study," *Journal of Hazardous Materials*, vol. 164, no. 2-3, pp. 1213–1222, 2009.

[52] S. Allen, G. Mckay, and K. Khader, "Intraparticle diffusion of a basic dye during adsorption onto sphagnum peat," *Environmental Pollution*, vol. 56, no. 1, pp. 39–50, 1989.

[53] S. K. Lagergren, "About the theory of so-called adsorption of soluble substances," *Sven. Vetenskapsakad. Handingarl*, vol. 24, pp. 1–39, 1898.

[54] S. Chien and W. Clayton, "Application of Elovich equation to the kinetics of phosphate release and sorption in soils," *Soil Science Society of America Journal*, vol. 44, no. 2, pp. 265–268, 1980.

[55] M. A. Al-Ghouti and M. M. Razavi, "Water reuse: brackish water desalination using *Prosopis juliflora*," *Environmental Technology & Innovation*, vol. 17, article 100614, 2020.

[56] N. Ayawei, A. N. Ebelegi, and D. Wankasi, "Modelling and interpretation of adsorption isotherms," *Journal of Chemistry*, vol. 2017, Article ID 3039817, 11 pages, 2017.

[57] M. A. Al-Ghouti and D. A. Da'ana, "Guidelines for the use and interpretation of adsorption isotherm models: a review," *Journal of Hazardous Materials*, vol. 393, article 122383, 2020.

[58] A. Günay, E. Arslankaya, and I. Tosun, "Lead removal from aqueous solution by natural and pretreated clinoptilolite: adsorption equilibrium and kinetics," *Journal of Hazardous Materials*, vol. 146, no. 1-2, pp. 362–371, 2007.

[59] G. Sarojini, S. V. Babu, and M. Rajasimman, "Adsorptive potential of iron oxide based nanocomposite for the sequestration of Congo red from aqueous solution," *Chemosphere*, vol. 287, article 132371, 2022.

[60] C. Lei, M. Pi, C. Jiang, B. Cheng, and J. Yu, "Synthesis of hierarchical porous zinc oxide (ZnO) microspheres with highly efficient adsorption of Congo red," *Journal of Colloid and Interface Science*, vol. 490, pp. 242–251, 2017.

[61] J. Hu, Z. Song, L. Chen, H. Yang, J. Li, and R. Richards, "Adsorption properties of MgO (111) nanoplates for the dye pollutants from wastewater," *Journal of Chemical & Engineering Data*, vol. 55, no. 9, pp. 3742–3748, 2010.

[62] Z. Wei, R. Xing, X. Zhang, S. Liu, H. Yu, and P. Li, "Facile template-free fabrication of hollow nestlike α-Fe_2O_3 nanostructures for water treatment," *ACS Applied Materials & Interfaces*, vol. 5, no. 3, pp. 598–604, 2013.

[63] X. Wang, Y. Zhong, T. Zhai et al., "Multishelled Co_3O_4-Fe_3O_4 hollow spheres with even magnetic phase distribution: synthesis, magnetic properties and their application in water treatment," *Journal of Materials Chemistry*, vol. 21, no. 44, pp. 17680–17687, 2011.

[64] M. S. Reddy, L. Sivaramakrishna, and A. V. Reddy, "The use of an agricultural waste material, Jujuba seeds for the removal of anionic dye (Congo red) from aqueous medium," *Journal of Hazardous Materials*, vol. 203, pp. 118–127, 2012.

[65] S. Al-Salihi, A. M. Jasim, M. M. Fidalgo, and Y. Xing, "Removal of Congo red dyes from aqueous solutions by porous γ-alumina nanoshells," *Chemosphere*, vol. 286, article 131769, 2022.

[66] C. Arab, R. El Kurdi, and D. Patra, "Zinc curcumin oxide nanoparticles for enhanced adsorption of Congo red: kinetics and adsorption isotherms study," *Materials Today Chemistry*, vol. 23, article 100701, 2022.

[67] Y. Pi, C. Duan, Y. Zhou et al., "The effective removal of Congo red using a bio-nanocluster: Fe_3O_4 nanoclusters modified bacteria," *Journal of Hazardous Materials*, vol. 424, article 127577, 2022.

[68] B. Aissa, L. Khezami, K. Taha et al., "Yttrium oxide-doped ZnO for effective adsorption of basic fuchsin dye: equilibrium, kinetics, and mechanism studies," *International journal of Environmental Science and Technology*, pp. 1–14, 2021.

[69] H. Zhang, J. Hu, J. Xie, S. Wang, and Y. Cao, "A solid-state chemical method for synthesizing MgO nanoparticles with superior adsorption properties," *RSC Advances*, vol. 9, no. 4, pp. 2011–2017, 2019.